

Quantum interference in graphene nanoconstrictions

Pascal Gehring^{1,*}, Hatef Sadeghi², Sara Sangtarash², Chit Siong Lau¹, Junjie Liu¹, Arzhang Ardavan³,
Jamie H. Warner¹, Colin J. Lambert², G. Andrew. D. Briggs¹, Jan A. Mol¹

¹*Department of Materials, University of Oxford, 16 Parks Road, Oxford OX1 3PH, United Kingdom*

²*Quantum Technology Centre, Physics Department, Lancaster University, Lancaster LA1 4YB, United Kingdom*

³*Clarendon Laboratory, Department of Physics, University of Oxford, Parks Road, Oxford OX1 3PU, United Kingdom*

*pascal.gehring@materials.ox.ac.uk

Abstract

We report quantum interference effects in the electrical conductance of chemical vapour deposited graphene nanoconstrictions fabricated using feedback controlled electroburning. The observed multi-mode Fabry-Pérot interferences can be attributed to reflections on potential steps inside the channel. Sharp anti-resonance features with a Fano line shape are observed. Theoretical modelling reveals that these Fano resonances are due to localised states inside the constriction, which couple to the delocalised states that also give rise to the Fabry-Pérot interference patterns. This study provides new insight into the interplay between two fundamental forms of quantum interference in graphene nanoconstrictions.

KEYWORDS: graphene, quantum interference, Fano resonance, break junction, Fabry-Pérot

A key feature of electron transport through single molecules and phase-coherent nanostructures is the appearance of transport resonances associated with quantum interference.[1] Examples include Breit-Wigner resonances, multi-path Fabry-Pérot resonances and Fano resonances. Fano resonances can be observed when a localised state interacts with a continuum of extended states and can lead to very steep gradients in the transmission. Unlike Breit-Wigner resonances, they are not life-time broadened

1
2
3 by coupling to the electrodes. The steep slope of Fano resonances makes them attractive for low-
4 power switching and for creating structures with high thermoelectric performance.[2] In what follows,
5 we report the first observation of Fano resonances in electroburnt graphene nanoconstrictions. In
6 addition to these Fano features, the conductance maps exhibit interference patterns which we attribute
7 to multi-mode Fabry-Pérot (FP) interferences. Theoretical modelling reveals that the Fano resonances
8 arise from interaction between the delocalised state giving rise to the Fabry-Pérot pattern and a
9 localised state inside the constriction.
10

11
12
13 Carbon-based nanostructures, such as metallic or semiconducting single carbon chains[3,4], graphene
14 nanoribbons and graphene nanoconstrictions are interesting platforms for the study of spintronics[5]
15 and might enable novel technological applications[6]. Graphene nanoconstrictions and nanogaps also
16 provide a robust platform for studying the electric[7], thermoelectric[8] and magnetic[9] properties of
17 single molecules. When sufficiently narrow, graphene nanoribbons can be used to build field-effect
18 transistors with an on/off ratio that can exceed 1000.[10] In very narrow constrictions, with a width
19 smaller than the electronic wavelength of electrons, quantum interference effects in analogy to
20 subwavelength optics are predicted[11,12]. Graphene nanoconstrictions have been fabricated by
21 means of electron beam lithography[13], gold break-junction etching masks[10], local gating[14] and
22 electroburning of graphene[15,16]. Electroburning has also been used to fabricate graphene quantum
23 dots with addition energies up to 1.6 eV, enabling the observation of Coulomb blockade at room
24 temperature[17]. In this study we use feedback-controlled electroburning to narrow down
25 lithographically-defined bowtie shaped graphene constrictions[18] and study their electronic transport
26 behaviour.
27

28
29
30 Our devices are fabricated from single-layer CVD-grown graphene[19] which we transfer onto a
31 Si/300nm SiO₂ wafer with pre-patterned 10 nm Cr / 70 nm Au contacts. We pattern the graphene into
32 a bowtie shape (see Figure 1a,b) using standard electron beam lithography and O₂ plasma etching.
33 The channel length L of the devices and the width W of the narrowest part of the constriction are 4 μm
34 and 200 nm, respectively (see Figure 1a). Our devices are p-doped with a Dirac point V_{Dirac} around 60
35 V (see Figure 1c). The single-layer nature of the graphene constriction is confirmed by the intensity
36
37
38
39
40
41
42
43
44
45
46
47
48
49
50
51
52
53
54
55
56
57
58
59
60

1
2
3 ratio $I(2D) / I(G) \gg 1$ of the Raman G and 2D peaks (see Figure 1d) and the fact that the 2D peak
4 consists of a single Lorentzian.[20,21] In addition, we observe a D and D' peak which we attribute to
5 the defective graphene edges formed during the plasma etching.[21] These defect peaks are not
6 present in bulk single-layer graphene samples.[19] To narrow down the constriction we use a
7 feedback-controlled electroburning technique in air, similar to the one described in Ref [18]. We
8 ramp-up a voltage applied between the source and drain contact while monitoring the current with a 5
9 kHz sampling rate (see Figure 1b). As soon as a drop in the current is detected, the voltage is quickly
10 ramped back to zero. This cycle is repeated until the low bias source-drain resistance of the device,
11 which is measured after each burning cycle, exceeds a threshold resistance of 500 M Ω . The feedback
12 conditions are adjusted for each burning cycle depending on the threshold voltage V_{th} at which the
13 drop in the previous cycle occurred. The current-voltage ($I - V_b$) traces of a typical electroburning
14 process are shown in Figure 1e, where the $I - V_b$ traces before electroburning and after the threshold
15 resistance is reached are coloured blue and red, respectively.
16
17
18
19
20
21
22
23
24
25
26
27
28
29

30 During electroburning, the constriction is narrowed down and as a result the resistance of the device
31 increases. At the final stage, the (only several atoms wide) constriction can break completely and a
32 nanometre sized gap is formed.[12] However, for many devices the threshold resistance is reached
33 before a gap is fully formed. In these cases, narrow graphene constrictions or small graphene islands
34 are left between the mesoscopic graphene leads. Graphene quantum dots formed in this manner have
35 been widely studied[15-17,22] as a possible platform for room temperature single-electron transistors.
36 In the following we discuss the details of the transport characteristics of empty graphenogaps,
37 quantum dots and nanoconstrictions recorded at $T = 4$ K in vacuum ($\sim 10^{-6}$ mbar).
38
39
40
41
42
43
44
45
46

47 The transport regime which we attribute to an empty gap is characterised by low currents and $I - V_b$
48 characteristics that can be fitted using the standard Simmons model[23] for tunnelling through a
49 single trapezoidal barrier between source and drain (see Figure 2a). In addition, the $I - V_b$
50 characteristics show no or a relatively small back gate dependence (see Figure 2b). We find gap sizes
51 of 0.5 – 2.5 nm for these junctions, making them a promising platform for single molecule
52 electronics.[7,24,25]
53
54
55
56
57
58
59
60

1
2
3 Devices in the weakly coupled quantum dot regime show suppressed current at low bias (see Figure
4 2c) and characteristic Coulomb diamonds as a function of bias and gate voltage (see Figure 2d). These
5 transport features are indicative of sequential electron tunnelling via a weakly coupled quantum dot
6 between source and drain.[26] From the size of the Coulomb diamonds we can extract addition
7 energies for these quantum dots ranging from 20 to 800 meV, comparable to those found by other
8 groups in similar systems.[13,15-17] The formation of graphene quantum dots during electroburning
9 process is the result of electron/hole localisation due to charge puddles and/or edge disorder as the
10 graphene channel gets narrower.[27] Theoretical calculations have also shown that localised states can
11 form along the edges of wedge-shaped nanoconstrictions.[28] Furthermore, it is possible that small
12 graphene islands on the order of several nm form, which are only weakly coupled to the graphene
13 leads.[17]

14
15
16
17
18
19
20
21
22
23
24
25
26 The conductance maps of strongly-coupled devices are dominated by “chess board”-like interference
27 patterns as shown in Figure 2f. In some samples we could observe a transition from this chess board
28 pattern to a Coulomb diamond regime at high positive gate voltages of $\gtrsim 40\text{V}$. This observation is
29 similar to results found in recent studies on short graphene junctions[29,30] and narrow graphene
30 constrictions[31]. In the latter, the chess board pattern was attributed to interference effects of
31 extended states in the source or drain graphene lead connecting the constriction.[31] In general,
32 interference effects occur on a length scale on the order of the phase coherence length, but can have
33 different origins. If the transport in the graphene sample is diffusive, i.e. when charge carriers are
34 predominantly scattered at random impurities like edge disorder, point defects or charge puddles,[27]
35 the origin of the interference pattern is most likely due to quantum interferences of different random
36 scattering paths (universal conductance fluctuations, UCFs). If the channel length is on the order of or
37 shorter than the mean free path of the carriers (quasi-ballistic transport regime), reflections in the
38 channel result in quasi-periodic multi-mode or collective and periodic single-mode Fabry-Pérot
39 interferences. Carriers can get reflected at the metal contacts[30] or at potential barriers formed by
40 intentional local doping.[32] Whether single- or multi-mode interference is observed strongly depends
41 on the detailed device geometry.[33]

1
2
3 Fabry-Pérot interference effects have previously been observed in 1D nanowires[34], carbon
4 nanotubes[35] and 2D graphene[30], while UCFs have been observed in mesoscopic single-[36], bi-
5 and tri-layer[37] and epitaxial graphene samples[38]. To distinguish between these different types of
6 quantum interference, the chess board conductance patterns need to be carefully analysed for hidden
7 periodicities.[30] From the characteristic energy spacing between single features in the conductance
8 maps and Fast Fourier Transforms (FFTs) of the data shown in Figure 2f (see Figure S6a and b in the
9 Supplementary Information) we can extract a typical energy spacing of 4 – 5 meV. Using a particle-
10 in-a-box approximation[30] we estimate the relevant length scale $L = \hbar v_F / (2E)$ to be between 400 nm
11 for the theoretical local density approximation limit of the Fermi velocity of $v_F = 0.8 \times 10^6$ m/s and 1.1
12 μm for a Fermi velocity of $v_F = 2.4 \times 10^6$ m/s measured for CVD graphene on a quartz substrate.[39]
13 This length scale corresponds to half the minimal distance over which the electrons remain phase
14 coherent, therefore we can infer a lower bound for the phase coherence length $L_\phi > 800$ nm in our
15 samples.[29] This value is similar to the value found for exfoliated graphene on SiO_2 [40], epitaxial
16 graphene[41] and CVD graphene[42]. For short and wide devices small incident angles dominate
17 (longitudinal modes) and resonances appear at $k_F L = n\pi$. [32] However, since our devices are not in the
18 limit $W/L \gg 1$, both longitudinal and transversal modes need to be considered. To model conductance
19 maps for different aspect ratios we have performed nearest-neighbour tight-binding calculations[33]
20 (see section S5 Supplementary Information). Our calculations confirm that for $W \gg L$ a periodic
21 interference pattern with high contrast can be observed. This is due to the fact that the energy of
22 transversal modes $E_W = \hbar v_F / (2W)$ gets negligibly small. The same holds for the 1D limit $W \rightarrow 0$,
23 where E_W goes to infinity. In both cases the transport is dominated by longitudinal modes only. In the
24 intermediate multi-mode regime, periodic longitudinal modes can still be observed in the FFT but
25 with much smaller contrast. Since the aspect ratio W/L of our devices is close to unity we expect that
26 the interference pattern shown in Figure 2b will only be quasi-periodic because of multi-mode
27 interferences. Moreover, the fact that the width W of the samples is not constant will cause the
28 transversal modes to become chaotic.[11]
29
30
31
32
33
34
35
36
37
38
39
40
41
42
43
44
45
46
47
48
49
50
51
52
53
54
55
56
57
58
59
60

1
2
3 Because the measured chess board pattern is only quasi-periodic, we cannot exclude UCFs as an
4 origin of the observed pattern. UCFs are normally most pronounced at low doping concentrations
5 when the electrochemical potential of graphene is close to the Dirac point.[30] This is unlikely to be
6 the case in our *p*-doped graphene junctions. In addition, the periodicity which we can correlate with
7 the geometry of the device is very similar for all devices investigated in this study, which makes
8 multi-mode Fabry-Pérot interferences a more likely mechanism to explain our data.
9
10

11
12
13
14
15
16 Next, we will investigate the microscopic origin of the FP reflections. Based on our assumption for
17 the Fermi velocity (see above) we estimate that carriers are coherently reflected on a length scale of \approx
18 1 μm . The visibility/intensity of FP interferences is determined by the reflectance of the potential
19 steps. Unipolar cavities have a small finesse and result in a small visibility $(G_{\text{max}} - G_{\text{min}}) / (G_{\text{max}} +$
20 $G_{\text{min}})$ since the conservation of pseudospin suppresses backscattering in graphene.[32] A smooth
21 bipolar potential step like a *pn* junction formed near a metal-graphene contact has a much higher
22 finesse and leads to pronounced resonance pattern.[32] However, since the length scale of less than 1
23 μm found above is much smaller than the channel length of 4 μm of our devices there need to be
24 additional potential steps inside the graphene channel apart from the metal contacts. From scanning
25 electron microscopy and micro Raman spectroscopy (see Sections S1 and S4 in the Supplementary
26 Information) we can infer that the local hole concentration within a region of several hundreds of nm
27 around the graphene constriction is increased during electroburning. The increase of hole doping of
28 graphene on SiO₂ annealed in air was intensively studied and attributed to doping by O₂ and moisture
29 and a change in the degree of coupling between graphene and SiO₂. [43] This increased p doping can
30 result in the formation of a *pp*⁺*p* junction in the central region of the devices (see Figure S6c and d in
31 the Supplementary Information). Possible resonance conditions are reflections between the gold
32 contact/the *pn* junction close to the gold contact and the *pp*⁺*p* junction or reflections within the *pp*⁺*p*
33 junction which all have a characteristic length scale of several hundreds of nm. This length scale is on
34 the order of the-mean-free path of charge carriers in our devices (see Supplementary Information),
35 which further corroborates our interpretation that the chess board pattern arises from FP interferences
36 rather than scattering at random impurities inside the channel. The visibility of the FP interferences
37
38
39
40
41
42
43
44
45
46
47
48
49
50
51
52
53
54
55
56
57
58
59
60

1
2
3 $(G_{\max} - G_{\min}) / (G_{\max} + G_{\min}) > 10\%$ is high in our devices, which indicates that the unipolar p^+p
4 interfaces need to have a sharp potential drop with $k_F d \ll 1$, where d is the length over which the
5 carrier density changes.[44] We estimate this length scale by calculating the Fermi vector using $n =$
6 k_F^2/π and the charge carrier concentration $n = C_g^2(V_g - V_{\text{Dirac}})^2/e^2$,[30] where C_g is the capacitance
7 of the back gate and e is the elementary charge. For $V_{\text{Dirac}} = 60$ V (see Figure 1c), d is on the order of
8 3 nm.

9
10
11
12
13
14
15
16 We only see interference patterns in nearly fully-burned devices and not directly after the first
17 electroburning steps. We attribute this to the decreasing conductance of the graphene constriction
18 during electroburning, which decreases the denominator in $(G_{\max} - G_{\min}) / (G_{\max} + G_{\min})$ and thus
19 increases the visibility of the interferences. Another possible explanation for the onset of interference
20 pattern after electroburning is the recrystallisation of the constriction,[45] which may lead to a higher
21 mean free path that is required for reflections on the μm scale. The interplay between reduced width
22 and reduced carrier density may also increase the factor λ/W , where $\lambda = hv_F/E$ is the wavelength of
23 the electrons. If this ratio becomes $\gtrsim 3 - 5$ the Fabry-Pérot interferences have a high contrast.[11]
24
25
26
27
28
29
30
31
32

33 We now turn to the sharp anti-resonances in the interference regime as shown in Figure 3a and b
34 (around $V_g = -18$ V) in some samples (see Supplementary Information for data of other samples). The
35 slope of this anti-resonance feature is different from the slopes of the multi-mode FP interference
36 patterns. Repeated thermal cycling from 4 K to room temperature did not change the slope and
37 position of the feature observed at 4K (see Figure S8). The feature consists of an anti-
38 resonance/resonance double-peak as shown in Figure 3c. This asymmetric curve has a distinct Fano
39 line shape,[46] which is the result of coherent interaction between a localised resonant state with a
40 delocalised background state.[1] Fano resonances have previously been observed in double donor
41 systems in nanoscale silicon transistors[47] and in bundles of single walled CNTs[48]. Fano
42 resonances are also predicted for single molecule systems, where a backbone state is coupled to the
43 leads and a pendant side-group is only coupled to the backbone but not to the leads.[1] In a graphene
44 constriction connected to mesoscopic graphene leads there are delocalised states that give rise to the
45 previously discussed FP pattern, and bound states e.g. localised along the edges due to edge
46
47
48
49
50
51
52
53
54
55
56
57
58
59
60

roughness, that give rise to Coulomb blockade at high positive gate voltages close to the Dirac point (see Figure 2f).[31] We attribute the observed Fano resonances to the coherent interaction between these states.

To estimate the coherent coupling strength between the localised and delocalised states in the graphene nanoconstriction, we fit the low bias current – gate voltage ($I - V_g$) traces to the Fano formula:[48,49]

$$G(\varepsilon) = G_{\text{non}} + G_{\text{res}} \frac{(\varepsilon + q)^2}{\varepsilon^2 + 1}, \quad (1)$$

where G_{res} is the coherent contribution to the conductance, q is the complex Fano factor,[50] $\varepsilon = 2(E - \varepsilon_s)/\Gamma_{\text{Fano}}$, ε_s and Γ_{Fano} are the energy and coupling strength of the resonant localised state and G_{non} is the conductance of the non-resonant channel. We model the non-resonant background as the sum of a constant offset G_{off} and a Breit-Wigner peak $A \frac{\Gamma^2}{\Gamma^2 + (E - \varepsilon_b)^2}$. This non-resonant background accounts for the conductance peak close to the observed anti-resonance feature. Fits to our data at different bias voltages using Equation (1) are shown as solid lines in Figure 3c. We find for a low bias of $V_b = 0.1$ mV: $\varepsilon_s = -18.3$ meV, $\text{Re}(q) = 0.3$, $\text{Im}(q) = 1.1$, $|q| = 1.1$, $\Gamma_{\text{Fano}} = 0.4$ meV, and a Breit-Wigner peak at $\varepsilon_b = -20.5$ meV with a coupling strength of $\Gamma = 1.1$ meV using a lever arm dE/dV_g of 1 meV/V extracted from the slope of the Fabry-Pérot interference pattern as depicted by the dotted black line in Figure 3a. The Fano factor q is a combined measure for the energetic detuning and the ratio of the transmission amplitudes of the resonant and the non-resonant channel.[49] For $q \rightarrow \infty$, the transport is dominated by the resonant channel and the line shape becomes that of a Breit-Wigner peak. For $q \rightarrow 0$ non-resonant transport dominates resulting in a symmetric dip in the conductance.[49] The value of $|q| = 1.1$ found in our experiments results in an asymmetric feature with characteristic Fano line-shape.[48] The width of $\Gamma_{\text{Fano}} = 0.4$ meV of the resonant state is similar to the values of 0.25 – 0.5 meV found for carbon nanotube bundles.[48] The Fano factor q decreases with increasing positive bias voltage (see inset in Figure 3c) which we attribute to a detuning of the energies of the localised state and the extended states. For large negative bias voltages the detuning

1
2
3 changes the Fano factor from 1 to a high value, and the transport is dominated by a resonant channel
4
5 resulting in a Breit-Wigner peak.
6

7
8 The slope of the Fano feature, as seen in Figure 3a, results from the electrostatic coupling of the
9
10 localised ‘pendant’ state to the gate and lead electrodes. Figure 4a, shows a tight-binding model of a
11
12 pendant state interacting with an extended ‘backbone’ state. A chain of 5 sites acts as the backbone,
13
14 while a single site coupled to the second site of the backbone serves as pendant group. Figure 4b
15
16 shows the calculated transmission coefficient $T(E)$ as a function of energy E . A Fano-resonance
17
18 appears at an energy of about 0.5 eV, which is associated with the site energy of the bound state. The
19
20 various transmission maxima are Fabry-Pérot resonances of the backbone channel. To calculate the
21
22 differential conductance characteristic $dI/dV_b(V_b, V_g)$ of the device for different gate voltages V_g , bias
23
24 and gate voltage dependent transmission coefficients $T(E, V_b, V_g)$ were calculated for two different
25
26 potential profiles, where i) the bias drops over the left and right contacts (Figure 4c); or ii) the bias
27
28 drops along the device channel (Figure 4d). In the case where the bias voltage drops across the
29
30 contacts (see Figure 4c), the on-site energies of the pendant group and the backbone are not
31
32 influenced by the applied bias voltage. As a consequence the two anti-resonance Fano lines have the
33
34 same slope as the Fabry-Pérot interference lines (see Figure 4e). In contrast, when the potential drops
35
36 over the channel (see Figure 4d), the slopes of the anti-resonance lines and the backbone resonances
37
38 become different (see Figure 4f). As a result of the asymmetry of the junction, one of the Fano lines
39
40 almost vanishes (see section S7 in the Supplementary Information for details). Comparing the
41
42 calculations in Figure 4e and f with the experimental data in Figure 3a, we can conclude that, firstly,
43
44 the investigated junctions are asymmetric and, secondly, that a considerable portion of the applied
45
46 voltage has to drop across the junction. In a more realistic model, where two hexagonal lattices are
47
48 connected to various scattering regions with and without pendant groups (see Figure 5), Fano
49
50 resonances can be only observed in junctions with pendant groups (see section S6 and S8 for more
51
52 details). Molecular-dynamics simulations and density functional theory calculations of different
53
54 atomic configurations during nanogap formation[12] further show that dangling carbon atoms and
55
56
57
58
59
60

1
2
3 edge disorder can lead to Fano resonance in the transmission spectra of partially burned graphene
4 nanogaps (see section S8 in the Supplementary Information).
5
6

7
8 In summary we investigated graphene nanoconstrictions fabricated by narrowing down bowtie shaped
9 graphene ribbons using a feedback controlled electroburning technique. In the case of weakly-coupled
10 constrictions, the transport is dominated by Coulomb blockade with addition energies up to 800 meV.
11
12 In the strongly coupled regime, we observe quasi-periodic chess board like pattern in the conductance
13 maps which we attribute to multi-mode Fabry-Pérot interferences of delocalised states whose length
14 scale agrees with two possible resonance conditions: reflections inside the current-annealed low-
15 doped part of the device or reflections between the electrical contacts and the low-doped part. In some
16 of the devices, we observe sharp anti-resonances features with a Fano line shape inside the
17 interference regime in agreement with our tight binding modelling. We attribute these features to
18 interferences between the extended states and localised states inside the constriction. Such sharp anti-
19 resonances have the potential to underpin the development of low-power switches, because the
20 transmission of the structure can be tuned by a small gate voltage. Moreover, the Mott formula
21 predicts that a high $d\ln G/dV_g$ should also result in a high Seebeck coefficient[51], making such
22 devices promising candidates for thermoelectric energy harvesting.
23
24
25
26
27
28
29
30
31
32
33
34
35
36
37
38
39
40
41
42
43
44
45
46
47
48
49
50
51
52
53
54
55
56
57
58
59
60

References

- 1 Lambert, C. J. Basic concepts of quantum interference and electron transport in single-
2 molecule electronics. *Chemical Society Reviews* **44**, 875-888, (2015).
- 3
- 4
- 5
- 6
- 7
- 8
- 9
- 10 2 Finch, C., Garcia-Suarez, V. & Lambert, C. Giant thermopower and figure of merit in single-
11 molecule devices. *Physical review b* **79**, 033405, (2009).
- 12
- 13
- 14 3 Rong, Y. M. & Warner, J. H. Wired Up: Interconnecting Two-Dimensional Materials with
15 One-Dimensional Atomic Chains. *Acs Nano* **8**, 11907-11912, (2014).
- 16
- 17
- 18 4 Chuvilin, A., Meyer, J. C., Algara-Siller, G. & Kaiser, U. From graphene constrictions to
19 single carbon chains. *New J Phys* **11**, (2009).
- 20
- 21
- 22 5 Son, Y. W., Cohen, M. L. & Louie, S. G. Half-metallic graphene nanoribbons. *Nature* **444**,
23 347-349, (2006).
- 24
- 25
- 26 6 Pezoldt, J. *et al.* Top gated graphene transistors with different gate insulators. *Physica Status*
27 *Solidi C: Current Topics in Solid State Physics, Vol 7, No 2* **7**, 390-393, (2010).
- 28
- 29
- 30 7 Mol, J. A. *et al.* Graphene-porphyrin single-molecule transistors. *Nanoscale*, (2015).
- 31
- 32 8 Sadeghi, H., Sangtarash, S. & Lambert, C. J. Electron and heat transport in porphyrin-based
33 single-molecule transistors with electro-burnt graphene electrodes. *Beilstein journal of*
34 *nanotechnology* **6**, 1413-1420, (2015).
- 35
- 36
- 37
- 38 9 Candini, A., Klyatskaya, S., Ruben, M., Wernsdorfer, W. & Affronte, M. Graphene
39 Spintronic Devices with Molecular Nanomagnets. *Nano Lett* **11**, 2634-2639, (2011).
- 40
- 41
- 42 10 Lu, Y. *et al.* High-On/Off-Ratio Graphene Nanoconstriction Field-Effect Transistor. *Small* **6**,
43 2748-2754, (2010).
- 44
- 45
- 46 11 Darancet, P., Olevano, V. & Mayou, D. Coherent Electronic Transport through Graphene
47 Constrictions: Subwavelength Regime and Optical Analogy. *Physical Review Letters* **102**,
48 (2009).
- 49
- 50
- 51
- 52 12 Sadeghi, H. *et al.* Conductance enlargement in picoscale electroburnt graphene nanojunctions.
53 *Proceedings of the National Academy of Sciences of the United States of America* **112**, 2658-
54 2663, (2015).
- 55
- 56
- 57
- 58
- 59
- 60

- 1
2
3 13 Ihn, T. *et al.* Graphene single-electron transistors. *Materials Today* **13**, 44-50, (2010).
4
5 14 Allen, M. T., Martin, J. & Yacoby, A. Gate-defined quantum confinement in suspended
6
7 bilayer graphene. *Nat Commun* **3**, (2012).
8
9 15 Moser, J. & Bachtold, A. Fabrication of large addition energy quantum dots in graphene.
10
11 *Applied Physics Letters* **95**, (2009).
12
13 16 Ki, D. K. & Morpurgo, A. F. Crossover from Coulomb Blockade to Quantum Hall Effect in
14
15 Suspended Graphene Nanoribbons. *Physical Review Letters* **108**, (2012).
16
17 17 Barreiro, A., van der Zant, H. S. J. & Vandersypen, L. M. K. Quantum Dots at Room
18
19 Temperature Carved out from Few-Layer Graphene. *Nano Lett* **12**, 6096-6100, (2012).
20
21 18 Lau, C. S., Mol, J. A., Warner, J. H. & Briggs, G. A. D. Nanoscale control of graphene
22
23 electrodes. *Physical Chemistry Chemical Physics* **16**, 20398-20401, (2014).
24
25 19 Wu, Y. M. A. *et al.* Large Single Crystals of Graphene on Melted Copper Using Chemical
26
27 Vapor Deposition. *Acs Nano* **6**, 5010-5017, (2012).
28
29 20 Sun, Z. Z. *et al.* Growth of graphene from solid carbon sources. *Nature* **468**, 549-552, (2010).
30
31 21 Ferrari, A. C. & Basko, D. M. Raman spectroscopy as a versatile tool for studying the
32
33 properties of graphene. *Nat Nanotechnol* **8**, 235-246, (2013).
34
35 22 Puczkarski, P. *et al.* Three-terminal graphene single-electron transistor fabricated using
36
37 feedback-controlled electroburning. *Applied Physics Letters* **107**, (2015).
38
39 23 Simmons, J. G. Generalized Formula for Electric Tunnel Effect between Similar Electrodes
40
41 Separated by a Thin Insulating Film. *J Appl Phys* **34**, 1793-1803, (1963).
42
43 24 Lau, C. S. *et al.* Redox-Dependent Franck–Condon Blockade and Avalanche Transport in a
44
45 Graphene–Fullerene Single-Molecule Transistor. *Nano Lett* **16**, 170-176, (2016).
46
47 25 Burzurí, E. *et al.* Sequential Electron Transport and Vibrational Excitations in an Organic
48
49 Molecule Coupled to Few-Layer Graphene Electrodes. *ACS Nano*, (2016).
50
51 26 Hanson, R., Kouwenhoven, L. P., Petta, J. R., Tarucha, S. & Vandersypen, L. M. K. Spins in
52
53 few-electron quantum dots. *Reviews of Modern Physics* **79**, 1217-1265, (2007).
54
55 27 Bischoff, D. *et al.* Localized charge carriers in graphene nanodevices. *Applied Physics*
56
57 *Reviews* **2**, 031301, (2015).
58
59
60

- 1
2
3 28 Muñoz-Rojas, F., Jacob, D., Fernández-Rossier, J. & Palacios, J. J. Coherent transport in
4
5 graphene nanoconstrictions. *Physical Review B* **74**, 195417, (2006).
6
7 29 Miao, F. *et al.* Phase-coherent transport in graphene quantum billiards. *Science* **317**, 1530-
8
9 1533, (2007).
10
11 30 Oksanen, M. *et al.* Single-mode and multimode Fabry-Perot interference in suspended
12
13 graphene. *Physical Review B* **89**, 121414, (2014).
14
15 31 Bischoff, D., Libisch, F., Burgdorfer, J., Ihn, T. & Ensslin, K. Characterizing wave functions
16
17 in graphene nanodevices: Electronic transport through ultrashort graphene constrictions on a
18
19 boron nitride substrate. *Physical Review B* **90**, (2014).
20
21 32 Rickhaus, P. *et al.* Ballistic interferences in suspended graphene. *Nat Commun* **4**, (2013).
22
23 33 Gunlycke, D. & White, C. T. Graphene interferometer. *Applied Physics Letters* **93**, (2008).
24
25 34 Kretinin, A. V., Popovitz-Biro, R., Mahalu, D. & Shtrikman, H. Multimode Fabry-Perot
26
27 Conductance Oscillations in Suspended Stacking-Faults-Free InAs Nanowires. *Nano Lett* **10**,
28
29 3439-3445, (2010).
30
31 35 Liang, W. J. *et al.* Fabry-Perot interference in a nanotube electron waveguide. *Nature* **411**,
32
33 665-669, (2001).
34
35 36 Morozov, S. V. *et al.* Strong suppression of weak localization in graphene. *Phys Rev Lett* **97**,
36
37 (2006).
38
39 37 Staley, N. E., Puls, C. P. & Liu, Y. Suppression of conductance fluctuation in weakly
40
41 disordered mesoscopic graphene samples near the charge neutral point. *Physical Review B* **77**,
42
43 (2008).
44
45 38 Berger, C. *et al.* Electronic confinement and coherence in patterned epitaxial graphene.
46
47 *Science* **312**, 1191-1196, (2006).
48
49 39 Hwang, C. *et al.* Fermi velocity engineering in graphene by substrate modification. *Scientific*
50
51 *Reports* **2**, (2012).
52
53 40 Ki, D. K., Jeong, D., Choi, J. H., Lee, H. J. & Park, K. S. Inelastic scattering in a monolayer
54
55 graphene sheet: A weak-localization study. *Physical Review B* **78**, (2008).
56
57
58
59
60

- 1
2
3 41 Lara-Avila, S. *et al.* Disordered Fermi Liquid in Epitaxial Graphene from Quantum Transport
4 Measurements. *Phys Rev Lett* **107**, (2011).
5
6
7 42 Baker, A. M. R. *et al.* Weak localization scattering lengths in epitaxial, and CVD graphene.
8
9 *Physical Review B* **86**, (2012).
10
11 43 Ryu, S. *et al.* Atmospheric Oxygen Binding and Hole Doping in Deformed Graphene on a
12 SiO₂ Substrate. *Nano Lett* **10**, 4944-4951, (2010).
13
14
15 44 Cheianov, V. V. & Fal'ko, V. I. Selective transmission of Dirac electrons and ballistic
16 magnetoresistance of n-p junctions in graphene. *Physical Review B* **74**, 041403, (2006).
17
18
19 45 Qi, Z. J. *et al.* Electronic Transport of Recrystallized Freestanding Graphene Nanoribbons.
20
21 *Acs Nano* **9**, 3510-3520, (2015).
22
23 46 Miroshnichenko, A. E., Flach, S. & Kivshar, Y. S. Fano resonances in nanoscale structures.
24
25 *Rev Mod Phys* **82**, 2257-2298, (2010).
26
27 47 Verduijn, J. *et al.* Coherent transport through a double donor system in silicon. *Applied*
28
29 *Physics Letters* **96**, (2010).
30
31 48 Babić, B. & Schönberger, C. Observation of Fano resonances in single-wall carbon
32
33 nanotubes. *Physical Review B* **70**, 195408, (2004).
34
35 49 Gores, J. *et al.* Fano resonances in electronic transport through a single-electron transistor.
36
37 *Physical Review B* **62**, 2188-2194, (2000).
38
39 50 Clerk, A. A., Waintal, X. & Brouwer, P. W. Fano resonances as a probe of phase coherence in
40
41 quantum dots. *Physical Review Letters* **86**, 4636-4639, (2001).
42
43 51 Cutler, M. & Mott, N. F. Observation of Anderson Localization in an Electron Gas. *Physical*
44
45 *Review* **181**, 1336-1340, (1969).
46
47
48
49
50
51
52
53
54
55
56
57
58
59
60

Acknowledgements

We thank the Royal Society for a Newton International Fellowship for J. A. M., the Agency for Science Technology and Research (A*STAR) for a studentship for C.S.L. and a University Research Fellowship for J. H. W. This work is supported by Oxford Martin School, the European Commission (EC) FP7 ITN “MOLESCO” (project no. 606728) and UK EPSRC (grant nos. EP/K001507/1, EP/J014753/1, EP/H035818/1 and EP/J015067/1). This project/publication was made possible through the support of a grant from Templeton World Charity Foundation. The opinions expressed in this publication are those of the author(s) and do not necessarily reflect the views of Templeton World Charity Foundation. The authors would like to thank D. Gunlycke for his help and the useful discussions and Y. Fan and J. Nägele for providing supporting transport data.

Captions

Figure 1. (a) False colour SEM image of a graphene constriction (grey) contacted by gold contacts (yellow). (b) Schematic of a graphene nanoconstriction device. (c) Conductance as a function of back gate voltage recorded at $V_b = 100$ mV of an as-prepared device. (d) Raman spectrum of the centre region of the graphene bow-tie after electroburning. (e) $I - V_b$ traces recorded during feedback-controlled electroburning. The first and last traces are shown in blue and red, respectively.

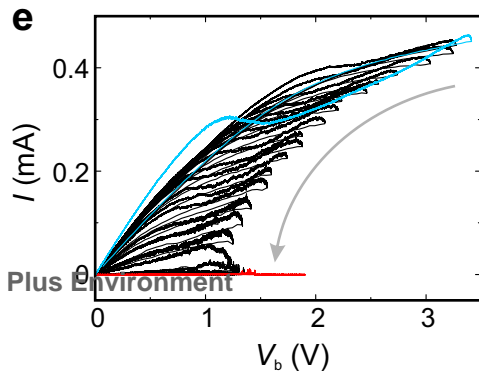
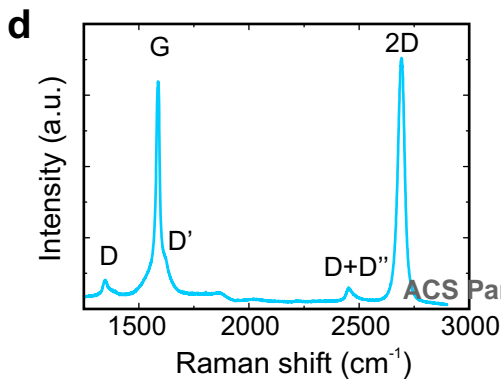
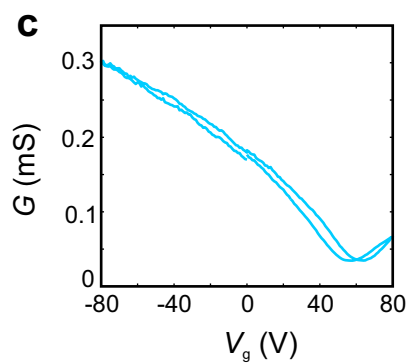
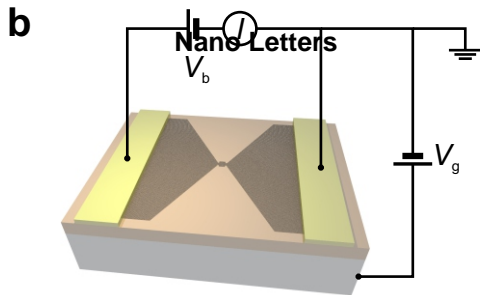
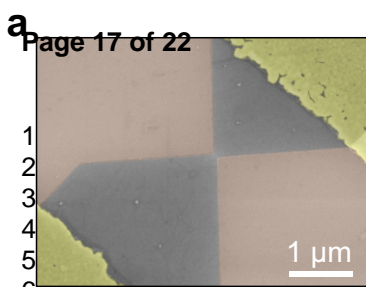
Figure 2. Nanostructures with different electronic behaviour formed during electroburning. (a) $I - V_b$ trace and (b) current map of an empty gap. (c) $I - V_b$ trace and (d) current map of a weakly coupled constriction showing sequential tunnelling. (e) $I - V_b$ trace and (f) conductance map of a strongly coupled constriction showing resonance effects. All data was recorded at $T = 4$ K under vacuum. The insets depict a scheme of the constriction.

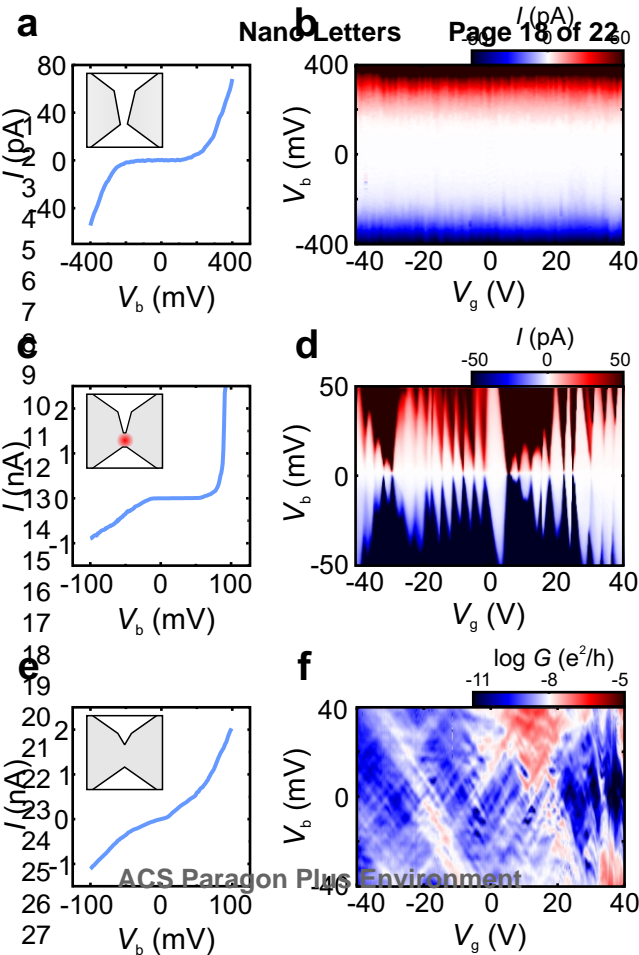
Figure 3. (a) Conductance map at $T = 4$ K of a strongly coupled constriction showing interference effects. A sharp anti-resonance feature around $V_g = -18$ V can be observed. The dotted line is used to extract the lever arm. (b) Gate traces for different bias voltages $0.1 \text{ mV} \leq V_b \leq 8 \text{ mV}$ in 0.2 mV steps of the data shown in (a). The curves are offset by $0.2 \times 10^3 e^2/h$ for clarity. (c) Gate traces at different

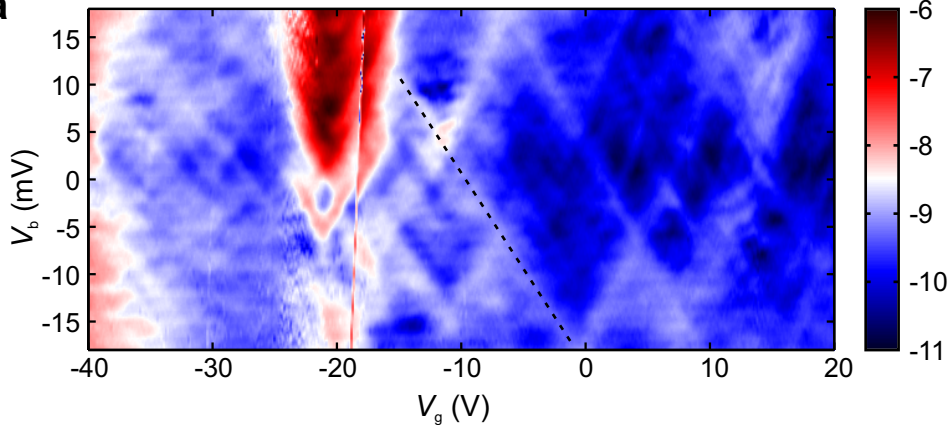
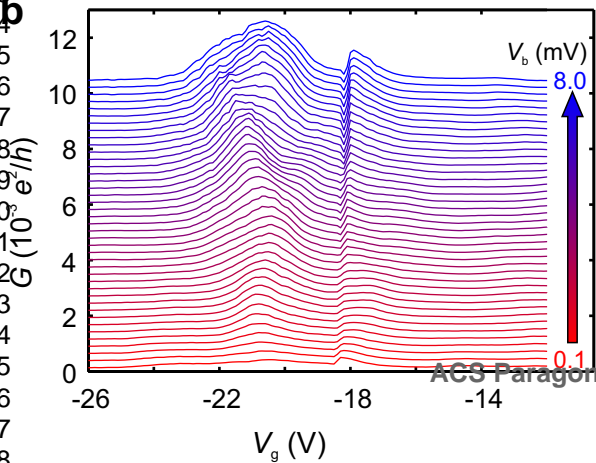
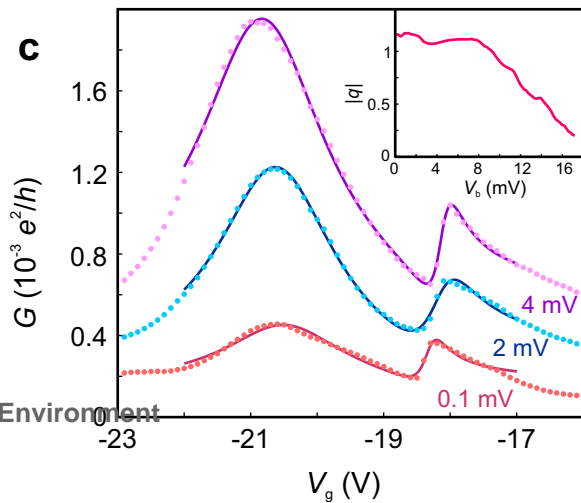
1
2
3 bias voltages (dotted lines) and fits using Equation 1 (solid lines). The inset shows the dependence of
4
5 the Fano factor $|q|$ as a function of the applied bias voltage.
6
7

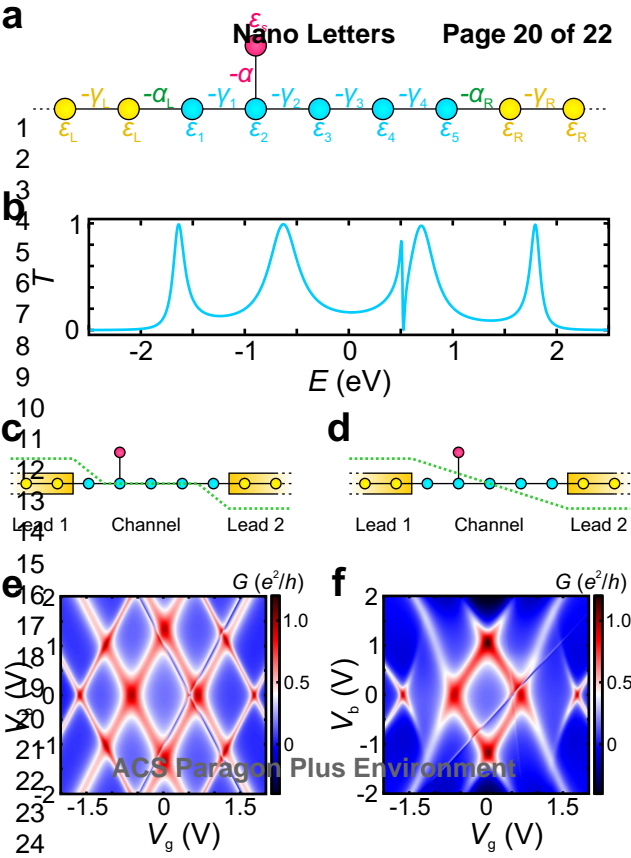
8 **Figure 4.** (a) Tight-binding model of a pendant state interacting with an extended ‘backbone’ state.
9
10 The backbone is described by a chain of 5 sites with on-site energies ε_{1-5} that are coupled by hopping
11
12 matrix elements $-\gamma_{1-4}$ and coupled to the leads via the outer most sites by hopping matrix elements
13
14 $-\alpha_L$ (on the left side) and $-\beta_R$ (on the right side). The pendant group with an on-site energy ε_s is
15
16 coupled to the second site of the backbone by a hopping matrix element $-\alpha$. (b) Calculated
17
18 transmission coefficient as a function of energy. (c), (d) Sketch of the potential profile where (c) the
19
20 bias drops over the left and right contacts and (d) the bias voltage drops along the device channel. (e),
21
22 (f) Corresponding conductance maps as a function of bias and gate voltage for the cases depicted in
23
24 (c), (d), respectively.
25
26

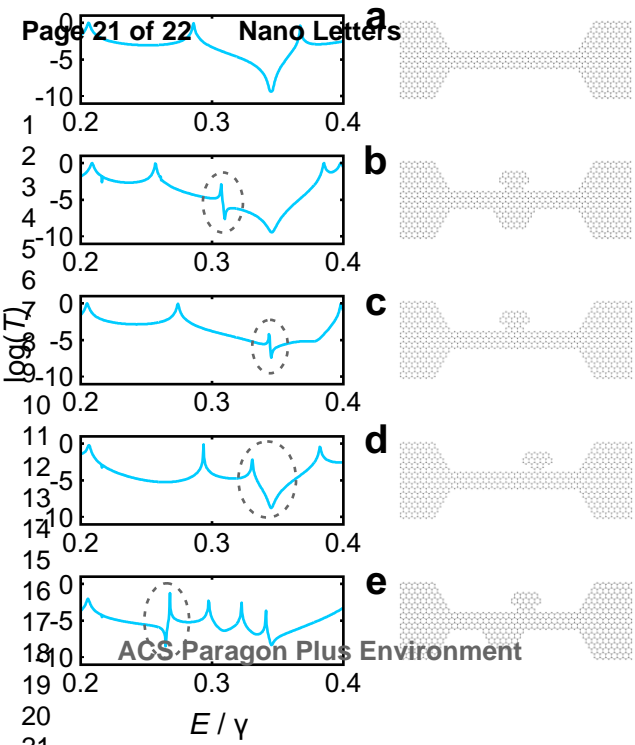
27 **Figure 5.** Transmission through graphene junctions. (a) Clean graphene ribbon connected to two
28
29 graphene electrodes, (b-e) graphene junctions with different shape and position of pendent groups.
30
31 The dotted circles indicate the position of Fano features.
32
33
34
35
36
37
38
39
40
41
42
43
44
45
46
47
48
49
50
51
52
53
54
55
56
57
58
59
60

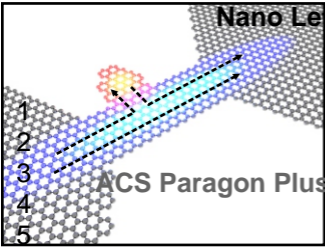




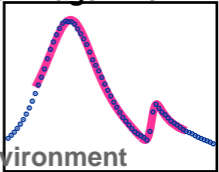
a**b****c**







Conductance



1
2
3
4
5

6

Gate voltage